

# Active Terahertz-Beam Deflection in a Double-Sided All-Dielectric Metadevice Modulated by both Polarization Rotation and Optical Pumping

Jiayue Liu,<sup>1</sup> Fei Fan<sup>1,2,\*</sup>, Zhiyu Tan,<sup>1</sup> Huijun Zhao,<sup>1</sup> Jierong Cheng,<sup>1</sup> and Shengjiang Chang<sup>2</sup>

<sup>1</sup>*Institute of Modern Optics, Nankai University, Tianjin Key Laboratory of Micro-scale Optical Information Science and Technology, Tianjin 300350, China*

<sup>2</sup>*Tianjin Key Laboratory of Optoelectronic Sensor and Sensing Network Technology, Tianjin 300350, China*

(Received 17 March 2023; revised 16 April 2023; accepted 1 May 2023; published 26 May 2023)

Active manipulation of the terahertz (THz) beam, especially beam deflection, is urgently required for wide THz applications. Although Pancharatnam-Berry (PB) metasurfaces can flexibly control the spatial phase distribution of circularly polarized waves, active power distribution and modulation between two conjugate spin beams are still challenging. Here, we demonstrate an all-dielectric metadevice consisting of an anisotropic metasurface layer and a PB metasurface layer etched on both sides of a silicon wafer. This structure develops a photonic spin-decoupling mechanism for spin-beam manipulation, which actively controls the power distribution between the two deflected spin beams by rotating the incident linearly polarized direction. The power-distribution ratio reaches 14.9:1 in the experiment. Moreover, the deflected beam can also be modulated by active switching via a laser pump, achieving an intensity-modulation depth of over 90%. The experimental modulation depth of the metadevice is 52% higher than that of the bare silicon wafer at the same pump power, which originates from the THz localized field enhancement and the strong dispersion effect of the PB structures. Therefore, this work provides a scheme for actively manipulating THz-beam deflection, realizing controllable wave-division multiplexing, power distribution, polarization control, and modulation.

DOI: 10.1103/PhysRevApplied.19.054086

## I. INTRODUCTION

Electromagnetic waves in the frequency range of 0.1–10 THz ( $1 \text{ THz} = 10^{12} \text{ Hz}$ ) are typically defined as terahertz (THz) waves, which belong to the transition region of the microwave and infrared bands. THz waves have important application value in wireless communication [1], radar [2], imaging [3], and spectroscopic detection [4]. Numerous THz control techniques and devices, including beam focusing, deflecting, steering, and polarization conversion, are key to advancing THz applications [5]. Among them, the deflection and scanning devices of the THz beam have been the focus of the THz community's attention [6–8]. However, traditional THz-deflection devices have difficulties in actively controlling their output power and energy distribution. Therefore, there is an urgent need for integrated and efficient THz-manipulation equipment.

With the development of metamaterials and metasurfaces, unprecedented degrees of freedom in the flexible control of THz waves are gained, and THz-beam manipulation is one of the hot spots on metasurfaces [9–11]. As periodically arranged subwavelength artificial elements,

the metasurfaces can flexibly control the amplitude, phase, polarization, and wave front of electromagnetic waves [12–14]. When the elements are arranged in a proper way to form a phased array, a variety of optical-field-manipulation functions can be obtained, such as holograms [15–17], abnormal beam deflection [18,19], and polarization manipulation [20–22]. Pancharatnam-Berry (PB) metasurfaces, which are composed of half-wave-plate (HWP) elements with a spatially rotating axis, can control the geometric phase of circularly polarized (CP) waves with two photonic spin states. Based on the unique properties of manipulating the CP waves [23–26], PB metasurfaces have been proposed for various functions, such as special beam generation [27–29], metalens [30], hologram [31,32], and anomalous reflection [33–36].

However, the fixed structure of the traditional PB metasurface cannot meet the requirements of dynamic manipulation of THz-beam deflection. Kim *et al.* demonstrated a gate-controlled THz PB metasurface that combined graphene to modulate the intensity of the anomalously refracted waves with a modulation depth of 28% [37]. Li *et al.* proposed an all-optical active PB-encoded metasurface to modulate the reflected THz beam at a single-frequency point of 1.09 THz with a modulation

\*fanfei@nankai.edu.cn

depth of 32% in amplitude [38]. Therefore, achieving an active THz-beam deflection device with high diffraction efficiency, wide scanning angle, and high modulation depth is still a great challenge. Moreover, the manipulation of CP waves based on PB metasurfaces is strictly symmetric when the linearly polarized (LP) beam is incident to the PB metasurfaces. The total power of the beam will be distributed evenly to a pair of conjugated spin beams, which are deflected to different sides with the same angle, so the active control of power distribution is difficult in the traditional PB metasurfaces.

Here, we demonstrate a double-sided all-dielectric metadevice that integrates both an anisotropic metasurface layer and a PB metasurface layer, as shown in Fig. 1(a). Due to the polarization-conversion effect of the anisotropic metasurface, this metadevice achieves a photonic spin-decoupling mechanism for PB phase structures. The active power distribution between the deflected right-handed circularly polarized (RCP) and left-handed circularly polarized (LCP) beams is realized by the polarization rotation of the incident LP wave. Moreover, optical pumping can also actively modulate the deflected beams based on the photogenerated-carrier effect of semiconductor Si, and the modulation depth can be significantly enhanced compared with the bare Si wafer without an artificial microstructure.

## II. RESULTS AND DISCUSSION

### A. Device design and fabrication

The double-sided metadevice is fabricated by photolithography and reactive-ion-beam etching on a high-resistance Si wafer with a thickness of 1 mm. As shown in Fig. 1(a), both sides have an etching depth of  $h_{\text{bar}} = 200 \mu\text{m}$ , and thus, the substrate has a thickness of  $h_{\text{sub}} = 600 \mu\text{m}$ . The front layer is an anisotropic metasurface composed of long rectangular columns with a length of  $l_1 = 680 \mu\text{m}$  and a width of  $w_1 = 82 \mu\text{m}$ , and this birefringent meta-atom has a period of  $p_1 = 800 \mu\text{m}$ . The back layer is a PB metasurface. The PB layer is composed of arranged meta-atoms with a period of  $p_2 = 200 \mu\text{m}$ , and groups of four meta-atoms along the  $x$  axis form a supercell. The four rectangular meta-atoms have the same shape and size with a length of  $l_2 = 57 \mu\text{m}$  and a width of  $w_2 = 160 \mu\text{m}$  but rotate sequentially with a step of  $\Delta\theta = 45^\circ$ . Both metasurface layers composed of rectangular columns can introduce an artificial birefringence phase shift in a pair of orthogonal directions, to realize the function of polarization conversion.

For the anisotropic layer, we hope to achieve a quarter-wave-plate (QWP) function in a broad-frequency band. If the LP wave is incident to a QWP with polarization angle  $\alpha$  relative to the long axis of the rectangular column, the

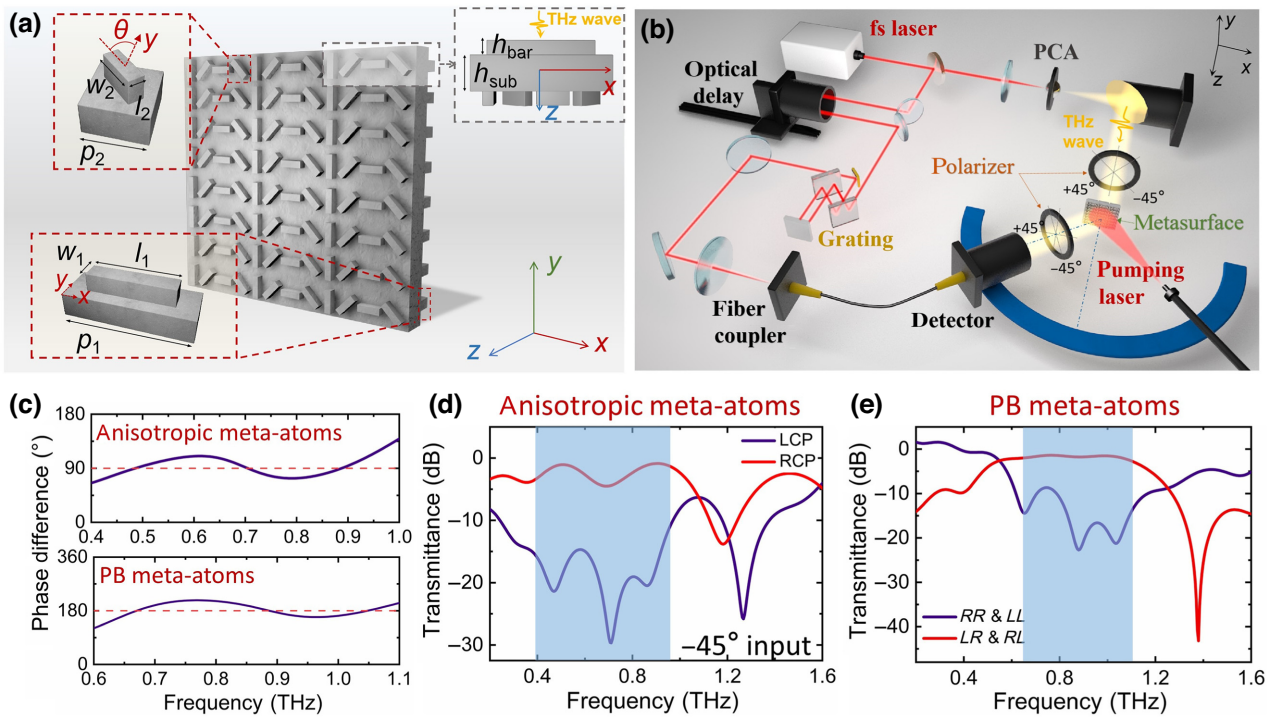


FIG. 1. (a) Geometric parameters of the metadevice. (b) Optical path diagram of the AR THz TDPS system. (c) Simulated birefringence phase shift of the anisotropic meta-atoms and PB meta-atoms in  $x$ - and  $y$ -orthogonal directions, (d) CP transmittance of the anisotropic meta-atoms for the LP wave input at a polarization angle of  $-45^\circ$ , and (e) CP transmittance of PB meta-atoms.

transmission matrix through the anisotropic metasurface layer can be expressed as follows:

$$\begin{bmatrix} E_{x\text{out}} \\ E_{y\text{out}} \end{bmatrix} = T_{\text{QWP}} \begin{bmatrix} E_{x\text{in}} \\ E_{y\text{in}} \end{bmatrix} = \begin{bmatrix} 1 & 0 \\ 0 & i \end{bmatrix} \begin{bmatrix} \cos \alpha \\ \sin \alpha \end{bmatrix} = \begin{bmatrix} \cos \alpha \\ i \sin \alpha \end{bmatrix}. \quad (1)$$

The LP wave (which can be regarded as the synthesis of a pair of equal-amplitude LCP and RCP waves) will be converted into elliptically polarized waves, and the ratio of LCP and RCP components is determined by polarization angle  $\alpha$ .

By optimizing the structure of the anisotropic meta-atoms, we obtain the birefringent phase shift of the anisotropic layer by the simulation, as shown in Fig. 1(c). The basic simulation method can be found in Sec. B of the Supplemental Material [39]. There is a broadband of about  $90^\circ$  phase difference in 0.4–0.95 THz, which means this anisotropic metasurface layer can work as a broadband QWP. As shown in Fig. 1(d), when  $\alpha = -45^\circ$ , the transmittance of the RCP component is much larger than that of LCP, indicating that the LP wave is converted into a RCP state in the broadband range.

For the PB layer, the function of the HWP is needed for PB meta-atoms. When the ideal case of  $t_x = t_y = 1$  is satisfied, for the CP wave incident to the meta-atoms, the output beam will be transformed with the form as follows [26]:

$$\begin{bmatrix} E_{L\text{out}} \\ E_{R\text{out}} \end{bmatrix} = T_{\text{PB}} \begin{bmatrix} E_{L\text{in}} \\ E_{R\text{in}} \end{bmatrix} = \begin{bmatrix} 0 & e^{2i\theta(x,y)} \\ e^{-2i\theta(x,y)} & 0 \end{bmatrix} \begin{bmatrix} E_{L\text{in}} \\ E_{R\text{in}} \end{bmatrix}. \quad (2)$$

The spin states will be converted and a pair of conjugate geometric phases,  $2i\theta$  and  $-2i\theta$ , are introduced into the LCP and RCP states, respectively.

Figure 1(c) shows the simulated birefringence phase shift of the designed PB meta-atoms. It can be seen that the phase difference is about  $180^\circ$  in the broadband range of 0.65–1.1 THz. The results of CP wave transmittance are shown in Fig. 1(e). The transmittances of the cross-polarized states  $LR$  and  $RL$  are much larger than the copolarized states  $LL$  and  $RR$  in the broadband range, indicating that the meta-atoms can work as an excellent broadband THz HWP.

As the desired phase can be obtained by rotating the meta-atoms by  $\theta$ , the gradient phase distribution of  $0$ – $360^\circ$  can be obtained by arranging the four meta-atoms with a step of  $\Delta\theta = 45^\circ$ . The conjugate phases of the LCP and RCP spin states can lead the wave front of the beam tilting to opposite sides, which realizes the deflection and separation of the LCP and RCP spin beams.

## B. Power distribution and intensity modulation by polarization rotation

Next, we discuss the active power distribution and intensity-modulation properties between the deflected beams affected by rotating polarization angle  $\alpha$  of the incident wave. The Jones matrix is used to describe the polarization-conversion mechanism of the double-sided metadevice composed of the front anisotropic metasurface and the back PB metasurface. A detailed derivation of the transmission matrix can be found in Sec. A of the Supplemental Material [39]. For an incident LP wave with polarization angle  $\alpha$ , the universal transmission matrix after passing through this double-sided metadevice can be obtained from

$$\begin{bmatrix} E_{x\text{out}} \\ E_{y\text{out}} \end{bmatrix} = \frac{1}{2} e^{-i2\theta} (\cos \alpha - \sin \alpha) \begin{bmatrix} 1 \\ i \end{bmatrix} + \frac{1}{2} e^{i2\theta} (\cos \alpha + \sin \alpha) \begin{bmatrix} 1 \\ -i \end{bmatrix}. \quad (3)$$

We can see that the LP wave will be converted into a RCP state when  $\alpha = +45^\circ$  and into a LCP state when  $\alpha = -45^\circ$  with conjugate geometric phases, and the ratio of LCP and RCP components can be tuned by rotating polarization angle  $\alpha$ . As shown in Fig. 2(a), the output LCP state and RCP state will be deflected to different sides in the  $x$  direction. Therefore, the power distribution of the deflected photonic spin beams can be dynamically controlled by using polarization rotation. Figure 2(b) shows the simulated electric field distributions of different spin states at 0.8 THz in the  $x$ - $z$  section at  $\alpha = +45^\circ$ , which can be regarded as an extreme case of the energy distribution between LCP and RCP state. It can be seen that, in this case, the energy is distributed into the RCP state and deflected to one side.

Figure 2(c) shows the frequency-dependent far-field deflection distribution in the simulation. The beam can be deflected to different sides in the broadband range of 0.7–1 THz at  $\pm 45^\circ$  input polarization angles. The  $\pm 45^\circ$  result has mirror symmetry. According to Snell's law, the correspondence between frequency  $f$  and deflection angle  $\varphi$  is  $\sin \varphi = c/(pf)$ , where  $p = 800 \mu\text{m}$  is the period of the metadevice and  $c$  is the speed of light in vacuum [19]. Therefore, the frequency range of 0.7–1 THz can achieve a broadband angle-dispersion range of  $\varphi = \pm 22^\circ$ – $\pm 32^\circ$ .

According to the above conclusions, we select a single frequency of 0.73 THz, corresponding to a deflection angle of  $\varphi = 31^\circ$ , to obtain the far-field transmittance varying with  $\alpha$ , as shown in Fig. 2(d). With the incident LP wave rotating from  $-45^\circ$  to  $+45^\circ$ , the transmittance gradually decays. The modulation effect of the THz-spin beam on this side from the “on” to “off” state is realized, showing the characteristic of dynamic intensity modulation of

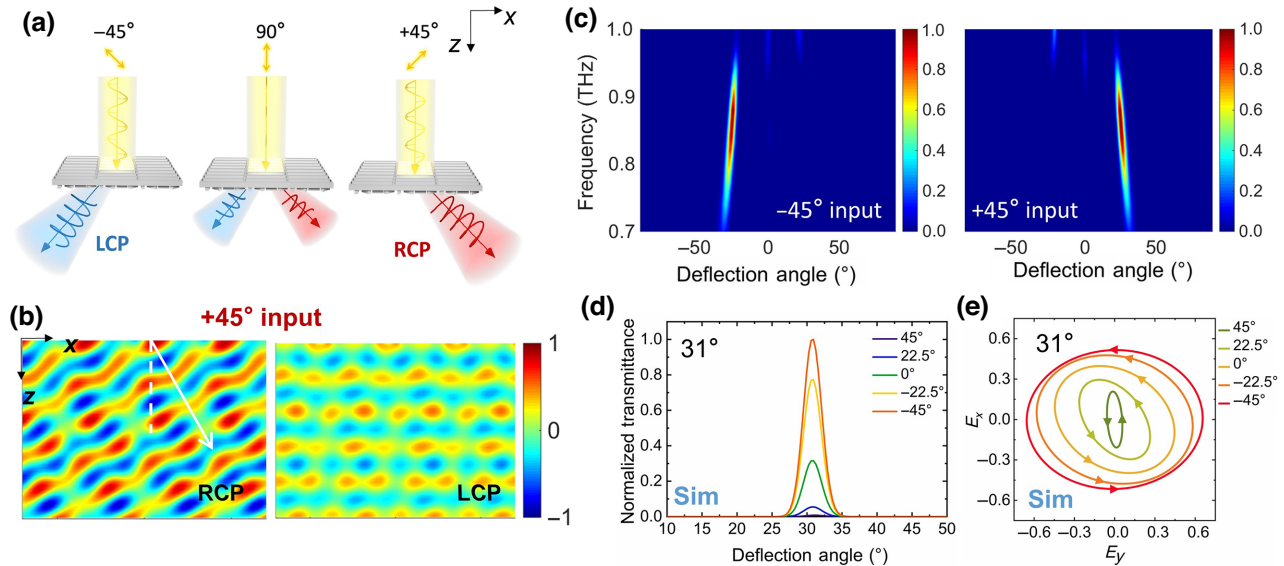


FIG. 2. (a) Mechanistic diagram of power distribution and intensity modulation by polarization rotation. (b) Simulated electric field distributions of spin states at 0.8 THz in the  $x$ - $z$  section at  $+45^\circ$  polarization angle, and (c) far-field deflection-efficiency maps with the angle-frequency distribution of the double-sided metadevice at  $+45^\circ$  and  $-45^\circ$  polarization angles. (d) Normalized far-field transmittance spectra and (e) polarization ellipses varying with the polarization angles at a deflection angle of  $31^\circ$ .

beam power. Figure 2(e) shows the polarization ellipses of the outgoing beam. When the beam is incident at a polarization angle of  $-45^\circ$ , the outgoing polarization ellipse is approximately circular, and gradually moves away from the CP state with the clockwise rotation of the polarization angle.

For the experimental measurements, an angle-resolved THz time-domain polarization spectroscopy (AR THz TDPS) system is utilized, as shown in Fig. 1(b). A detailed description of the experimental system and the signal-processing methods can be found in Sec. C of the Supplemental Material [39]. In the experiment, one side of the THz signal is measured to explore the power-distribution function by polarization rotation, and different deflection angles  $\varphi$  corresponding to different frequencies are selected for analysis. Polarization angle  $\alpha$  is controlled from  $-45^\circ$  to  $+45^\circ$  with a rotating step of  $22.5^\circ$  to obtain the transmittance spectra.

As shown in Fig. 3(a), when the LP wave rotates from  $-45^\circ$  to  $+45^\circ$ , the maximum values of the transmission peak gradually drop to a lower value at deflection angles of  $\varphi = 28^\circ$  and  $31^\circ$ , which complies with the modulation rule in the simulation. However, at a deflection angle of  $25^\circ$ , the peak value still has a large value when  $\alpha = +45^\circ$ , even though the rule of decreasing peak value is still satisfied. Figure 3(b) shows the polarization ellipses corresponding to the transmission signal. For deflection angle  $\varphi = 31^\circ$ , the polarization state of the outgoing beam is approximately a CP state at  $\alpha = -45^\circ$  and gradually moves away from the CP state with rotation of the polarization angle, which is similar to the simulation results. However, for a deflection

angle of  $\varphi = 25^\circ$ , the polarization state of the outgoing beam significantly deviates from the CP state.

According to the above experimental results, we know that polarization rotation has a good modulation effect at deflection angles of  $\varphi = 28^\circ$  and  $31^\circ$ , with a deviation at  $25^\circ$ . The reason is that, for the frequency components corresponding to  $28^\circ$  and  $31^\circ$ , the phase difference introduced by the double-sided metadevice matches the phase conditions of QWP and HWP discussed in Sec. II A. Therefore, polarization rotation can control the conversion of different spin states well. However, the phase difference introduced at  $25^\circ$  has a large deviation. Hence, the phase is difficult to match perfectly in the broadband range in practical devices. Figure 3(d) shows the transmittance spectra detected only in the  $y$ -axis direction at different deflection angles. The transmission signal can be dispersed in the range of  $23^\circ$ – $32^\circ$ , which verifies the broadband characteristics of the metadevice.

To characterize the power-distribution performance of this polarization-dependent metadevice, we define the power-distribution ratio ( $R_p$ ) as follows:  $R_p = T_{r0}/T_r$ , where  $T_{r0}$  and  $T_r$  are the intensity transmittance at polarization angles of  $-45^\circ$  and  $+45^\circ$ , respectively. The power-distribution ratios at three deflection angles are calculated as shown in Fig. 3(c). The ratios of the THz signal at  $28^\circ$  and  $31^\circ$  deflection angles reach 10.2 and 14.9, respectively. This indicates that polarization rotation has a high modulation sensitivity, and the energy is almost transferred to the deflected spin state on the other side. When the polarization angle rotates between  $+45^\circ$  and  $-45^\circ$ , the THz energy is freely arranged on the positive and negative deflection

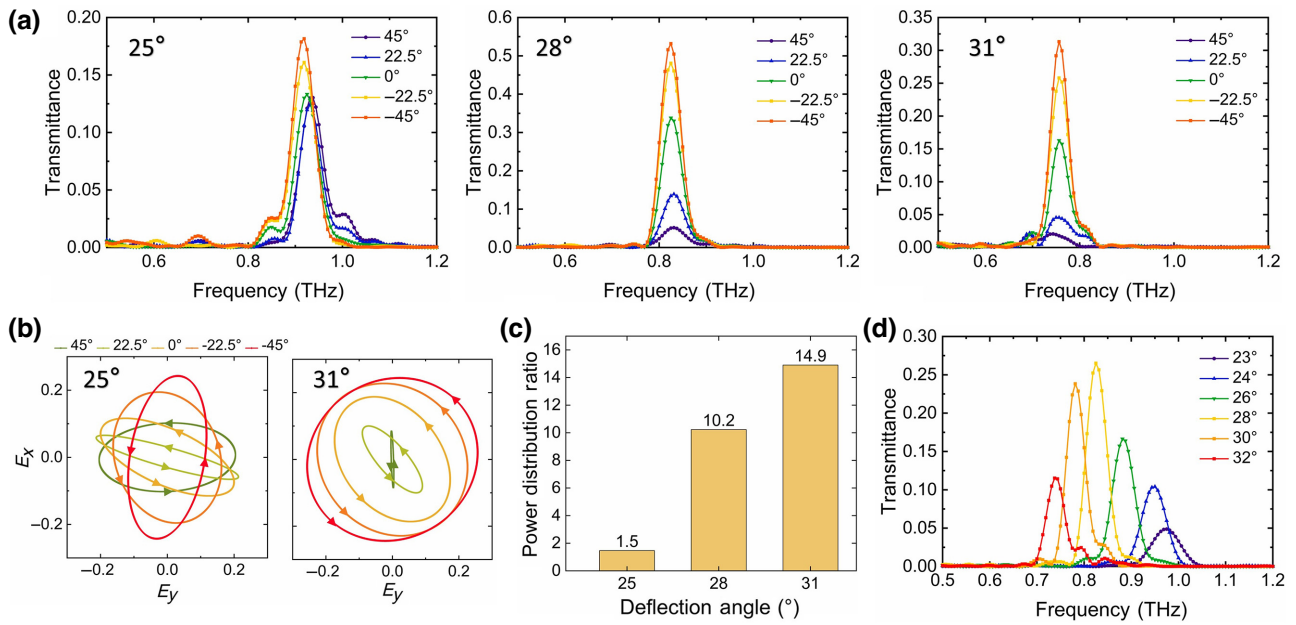


FIG. 3. (a) Experimental transmittance spectra varying with deflection angle  $\varphi = 25^\circ, 28^\circ$ , and  $31^\circ$ . (b) Polarization ellipses varying with  $\varphi = 25^\circ$  and  $31^\circ$ . (c) Power-distribution ratios at  $\varphi = 25^\circ, 28^\circ$ , and  $31^\circ$ . (d) Experimental transmittance spectra at different deflection angles.

angles in the form of RCP and LCP states, respectively. Therefore, this composite metadevice demonstrates a photonic spin-decoupling mechanism for the PB structure combined with polarization conversion of the anisotropic metasurface layer.

### C. Optical pumping modulation

Next, we use optical pumping for further switching modulation of the deflected THz-spin beam based on the photogenerated carrier effect in the semiconductor, Si, of this metadevice. Figure 4(a) is a schematic diagram of optical pumping modulation. When the 808-nm laser irradiates the surface of the Si structure, electrons in Si will be excited and transit from the valence band to the conduction band to form a large number of electron-hole pairs. Therefore, the carrier concentration on the surface of Si will increase rapidly, leading to the formation of a metal-like reflection layer of THz waves. The original deflected beam will weaken or even disappear because of the metal-like reflection layer. The Drude model is appropriate to analyze the interaction of Si material with THz waves under laser pumping; this can be found in Sec. B of the Supplemental Material [39].

To simulate the modulation effect of the optical pumping on THz waves, we used the conductive three-dimensional model in the finite-difference time-domain software SOLUTION to create the metal-like layer material and set the thickness to 0.5  $\mu\text{m}$ . For the PB metasurface layer, most of the side walls of the column cannot be illuminated by

a laser because of the large depth-to-width ratio, so we set only the metal-like layer to cover the top of the column for each PB meta-atom and the remaining bottom surface on the substrate to model the excited region, as shown in Fig. S1 of the Supplemental Material [39]. In the model, we define  $\varepsilon_\infty = 11.7$ , and conductivity  $\sigma$  as a variable to simulate the change of laser power. Conductivity  $\sigma$  in the model is proportional to the carrier concentration of Si, as described in Eq. (S11) of the Supplemental Material [39], and the laser pump excites the photocarriers in Si. Therefore, the change of conductivity in the simulation is consistent with the change of laser pump power in the experiment.

The simulated transmittances varying with the conductivities from 0 to  $2 \times 10^4$  S/m at deflection angle  $\varphi = 31^\circ$  of the metadevice are shown in Fig. 4(b). The transmittance peak value gradually decreases with an increase of the conductivity. For bare Si as a contrast, we set the metal-like layer on one of the surfaces of the Si wafer. The simulation results of bare Si are shown in Fig. 4(c), which shows a similar modulation rule to that of the metadevice.

The simulated electric field distributions near the surface of the bare Si wafer and PB metasurface layer at 0.8 THz in the  $x$ - $z$  section are shown in Figs. 4(d) and 4(e), respectively. When there is no optical pumping, conductivity  $\sigma$  of the metal-like layer is set to 0 S/m, and the THz wave can propagate through the surface of Si. When  $\sigma$  is increased to  $10^5$  S/m, most of the energy is reflected back to the interior of the bare Si wafer and metadevice. In contrast to unstructured Si, the metal-like layer on the PB

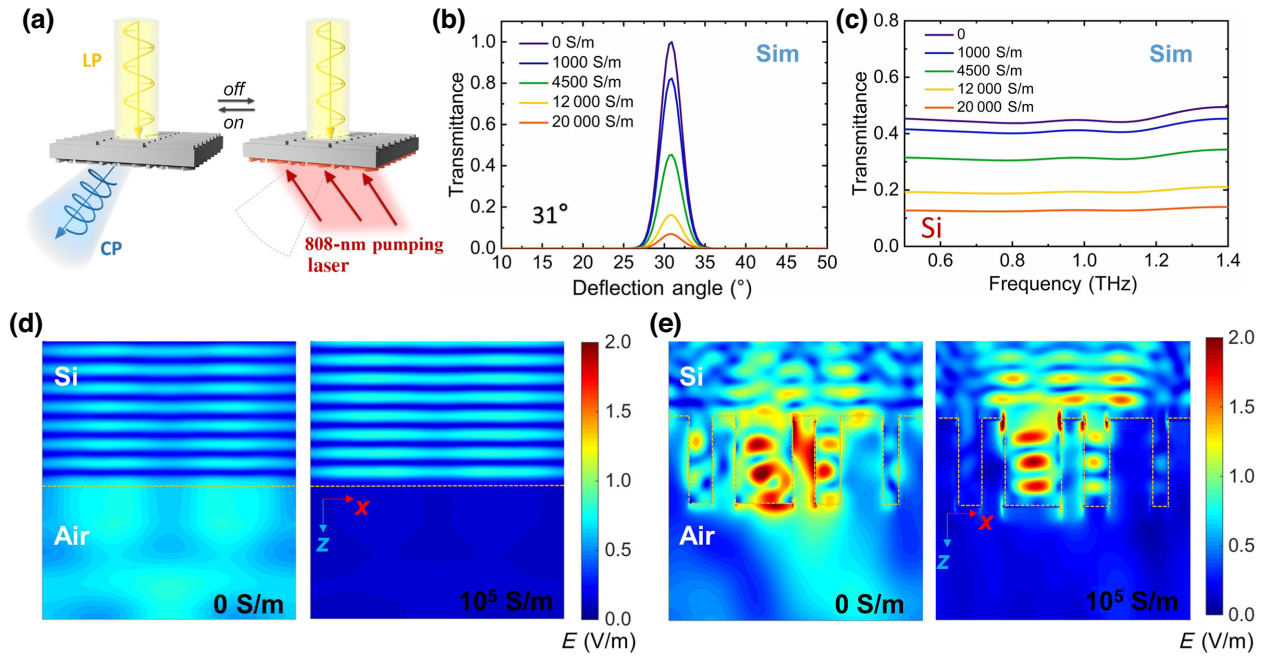


FIG. 4. (a) Mechanistic diagrams of optical pumping modulation. (b) Simulated normalized far-field transmittance spectra of the metadevice at a deflection angle of  $31^\circ$ , and (c) transmittance spectra of the Si wafer varying with conductivity. Simulated electric field distributions near the lower surface of (d) Si wafer and (e) metadevice at 0.8 THz in the  $x$ - $z$  section.

metasurface is structured to form rectangular strips at the top of the column and complementary rectangular holes at the bottom of the column. The PB meta-atom microstructure produces strong localized field enhancement, and field-localized hotspots are generated at the edge of the

structured metal-like layer at  $\sigma = 10^5$  S/m, as shown in Fig. 4(e). This physical phenomenon effectively strengthens the interaction between the incident THz wave and photon-generated carriers and improves the modulation effect of optical pumping.

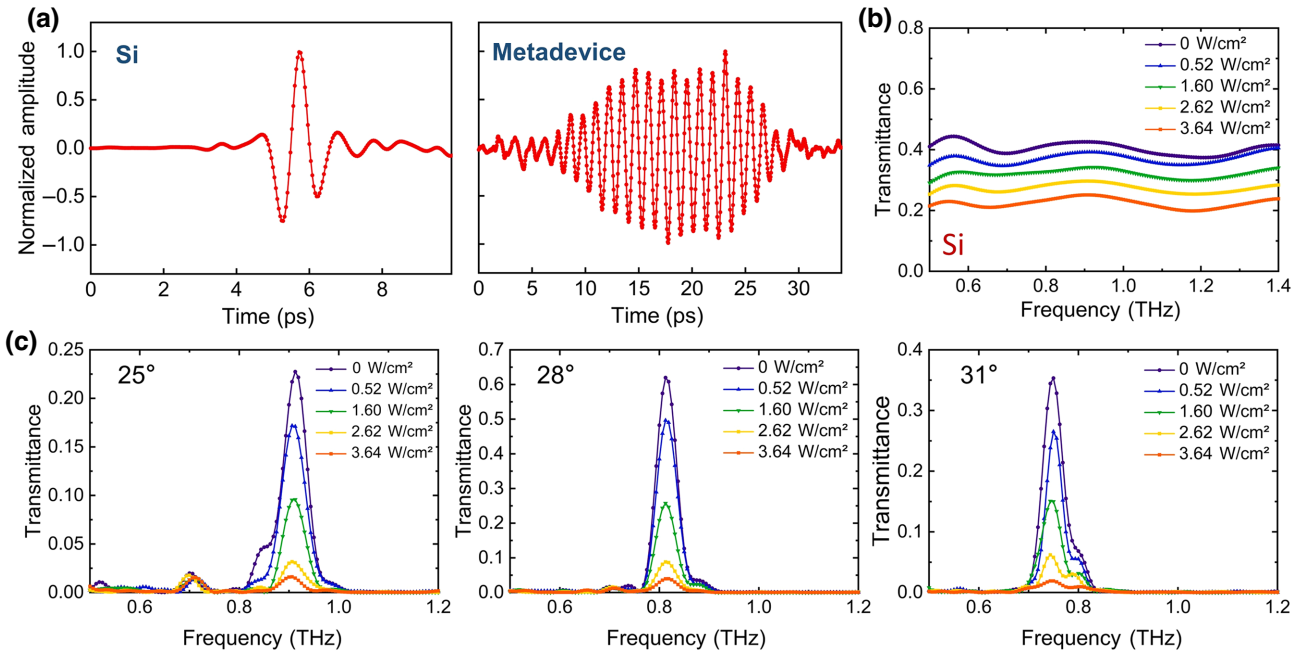


FIG. 5. (a) Experimental time-domain signals of bare Si wafer and metadevice. Transmittance spectra of (b) the metadevice at deflection angles of  $25^\circ$ ,  $28^\circ$ , and  $31^\circ$  and (c) bare Si wafer varying with pump-power density.

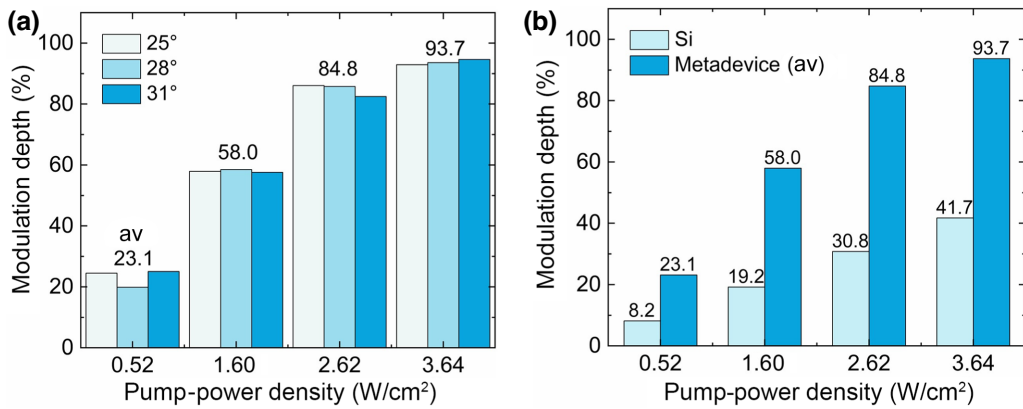


FIG. 6. (a) Optical-pumping-modulation depth of the metadevice at deflection angles of 25°, 28°, and 31° at different pump-power densities. (b) Comparison of the modulation depth of the Si wafer and metadevice at different pump-power densities.

In the experiment, we irradiate the PB metasurface layer of the metadevice and the bare Si wafer at a small tilt angle by different laser power densities. Figure 5(a) shows the time-domain spectral signals of the THz waves after passing through bare Si and the metadevice. The strong time-dispersion effect of the PB phase structure makes a very wide envelope and the delay of the THz time-domain signal through the metadevice. Hence, the THz wave can more fully interact with the metadevice structure, facilitating the enhancement of the modulation effect compared to bare Si. Figure 5(c) shows the transmittance spectra of the metadevice at three deflection angles of 25°, 28°, and 31° when  $\alpha = -45^\circ$ . The intensity transmittances at three deflection angles all gradually decrease with an increase of the pump-power density. Figure 5(b) shows that the Si wafer is modulated over a wide band, but the modulation depth is significantly lower than that of the metadevice.

The optical-pumping-modulation depth is defined as  $M_p = (T_{p0} - T_p)/T_{p0}$ , where  $T_{p0}$  is the intensity transmittance without pumping and  $T_p$  is the intensity transmittance at different pump-power densities. First, the optical-pumping-modulation depths at different pump-power densities at three deflection angles are calculated, as shown in Fig. 6(a). Optical pumping has almost the same modulation depth at the same pump-power density for different deflection angles. At a laser-power density of 3.64 W/cm<sup>2</sup>, the average modulation depth of the signal is up to 93.7%. Then the modulation depth of the unstructured Si wafer is also calculated and compared with the average modulation depth of the metadevice, as shown in Fig. 6(b). It can be seen that, under the same laser-power density, optical pumping has a better modulation effect for the metadevice compared with bare Si. The average modulation depth of the PB metasurface is 52% higher than that of flat Si wafers at a laser-power density of 3.64 W/cm<sup>2</sup>, which is attributed to the THz localized field enhancement and strong dispersion effect.

### III. CONCLUSION

Here, we demonstrate a double-sided all-dielectric metadevice composed of an anisotropic metasurface layer and a PB metasurface layer. Active modulation of THz-beam deflection is realized by combining the methods of polarization rotation and optical pumping. Some conclusions can be drawn. (1) The anisotropic layer and PB layer achieve 90° and 180° birefringent phase shifts, respectively, both in the broad-frequency band of 0.7–1 THz, so the deflection beams are widely dispersed in the spatial angle range of ±23° to ±32°. (2) The active power distribution between the deflected conjugate spin states can be realized based on polarization conversion in the anisotropic layer and the spin-beam-separation effect in the PB layer. The experimental results show that the power-distribution ratio reaches 14.9 at a deflection angle of 31°. (3) The pumping laser can realize active switching modulation of the deflected spin beams, and the modulation depth is 52% higher than that of the bare Si wafer due to the THz localized field enhancement and strong dispersion effect. Therefore, this work provides a scheme of actively manipulating the THz-beam deflection with controllable wave-division multiplexing, power distribution, and modulation, which has potential applications in THz wireless communication, radar, and imaging.

### ACKNOWLEDGMENTS

This work is supported by the National Natural Science Foundation of China (Grants No. 61831012 and No. 61971242) and the National Key Research and Development Program of China (Grant No. 2017YFA0701000).

- [1] T. Nagatsuma, G. Ducournau, and C. C. Renaud, Advances in terahertz communications accelerated by photonics, *Nat. Photonics* **10**, 371 (2016).

- [2] A. G. Davies, A. D. Burnett, W. Fan, E. H. Linfield, and J. E. Cunningham, Terahertz spectroscopy of explosives and drugs, *Mater. Today* **11**, 18 (2008).
- [3] P. U. Jepsen, D. G. Cooke, and M. Koch, Terahertz spectroscopy and imaging—modern techniques and applications, *Laser Photonics Rev.* **5**, 124 (2011).
- [4] A. B. True, K. Schroeck, T. A. French, and C. A. Schmuttenmaer, Terahertz spectroscopy of histidine enantiomers and polymorphs, *J. Infrared, Millimeter, Terahertz Waves* **32**, 691 (2011).
- [5] X. Fu, F. Yang, C. Liu, X. Wu, and T. J. Cui, Terahertz beam steering technologies: From phased arrays to field-programmable metasurfaces, *Adv. Opt. Mater.* **8**, 1900628 (2020).
- [6] L. Liu, X. Zhang, M. Kenney, X. Su, N. Xu, C. Ouyang, Y. Shi, J. Han, W. Zhang, and S. Zhang, Broadband metasurfaces with simultaneous control of phase and amplitude, *Adv. Mater.* **26**, 5031 (2014).
- [7] X. Zhang, Z. Tian, W. Yue, J. Gu, S. Zhang, J. Han, and W. Zhang, Broadband terahertz wave deflection based on C-shape complex metamaterials with phase discontinuities, *Adv. Mater.* **25**, 4567 (2013).
- [8] M. Liu, Q. Yang, A. A. Rifat, V. Raj, A. Komar, J. Han, M. Rahmani, H. T. Hattori, D. Neshev, D. A. Powell, and I. V. Shadrivov, Deeply subwavelength metasurface resonators for terahertz waveform manipulation, *Adv. Opt. Mater.* **7**, 1900736 (2019).
- [9] H. W. Tian, H. Y. Shen, X. G. Zhang, X. Li, W. X. Jiang, and T. J. Cui, Terahertz metasurfaces: Toward multifunctional and programmable wave manipulation, *Front. Phys.* **8**, 584077 (2020).
- [10] H. T. Chen, J. F. O’Hara, A. K. Azad, and A. J. Taylor, Manipulation of terahertz radiation using metamaterials, *Laser Photonics Rev.* **5**, 513 (2011).
- [11] T. J. Cui, M. Q. Qi, X. Wan, J. Zhao, and Q. Cheng, Coding metamaterials, digital metamaterials and programmable metamaterials, *Light: Sci. Appl.* **3**, e218 (2014).
- [12] W. J. Padilla, D. N. Basov, and D. R. Smith, Negative refractive index metamaterials, *Mater. Today* **9**, 28 (2006).
- [13] R. Degl’Innocenti, H. Lin, and M. Navarro-Cía, Recent progress in terahertz metamaterial modulators, *Nanophotonics* **11**, 1485 (2022).
- [14] T. J. Cui, L. Li, S. Liu, Q. Ma, L. Zhang, X. Wan, W. X. Jiang, and Q. Cheng, Information metamaterial systems, *iScience* **23**, 101403 (2020).
- [15] G. Zheng, H. Muhlenbernd, M. Kenney, G. Li, T. Zentgraf, and S. Zhang, Metasurface holograms reaching 80% efficiency, *Nat. Nanotechnol.* **10**, 308 (2015).
- [16] Z.-L. Deng and G. Li, Metasurface optical holography, *Mater. Today Phys.* **3**, 16 (2017).
- [17] L. Li, T. Jun Cui, W. Ji, S. Liu, J. Ding, X. Wan, Y. Bo Li, M. Jiang, C. W. Qiu, and S. Zhang, Electromagnetic reprogrammable coding-metasurface holograms, *Nat. Commun.* **8**, 197 (2017).
- [18] S. Sun, Q. He, S. Xiao, Q. Xu, X. Li, and L. Zhou, Gradient-index meta-surfaces as a bridge linking propagating waves and surface waves, *Nat. Mater.* **11**, 426 (2012).
- [19] N. Yu, P. Genevet, M. A. Kats, F. Aieta, J. P. Tetienne, F. Capasso, and Z. Gaburro, Light propagation with phase discontinuities: Generalized laws of reflection and refraction, *Science* **334**, 333 (2011).
- [20] N. K. Grady, J. E. Heyes, D. R. Chowdhury, Y. Zeng, M. T. Reiten, A. K. Azad, A. J. Taylor, D. A. Dalvit, and H. T. Chen, Terahertz metamaterials for linear polarization conversion and anomalous refraction, *Science* **340**, 1304 (2013).
- [21] J. Zi, Q. Xu, Q. Wang, C. Tian, Y. Li, X. Zhang, J. Han, and W. Zhang, Antireflection-assisted all-dielectric terahertz metamaterial polarization converter, *Appl. Phys. Lett.* **113**, 101104 (2018).
- [22] H. Zhang, X. Zhang, Q. Xu, Q. Wang, Y. Xu, M. Wei, Y. Li, J. Gu, Z. Tian, C. Ouyang, X. Zhang, C. Hu, J. Han, and W. Zhang, Polarization-independent all-silicon dielectric metasurfaces in the terahertz regime, *Photonics Res.* **6**, 24 (2018).
- [23] X. Yin, Z. Ye, J. Rho, Y. Wang, and X. Zhang, Photonic spin Hall effect at metasurfaces, *Science* **339**, 1405 (2013).
- [24] M. Jia, Z. Wang, H. Li, X. Wang, W. Luo, S. Sun, Y. Zhang, Q. He, and L. Zhou, Efficient manipulations of circularly polarized terahertz waves with transmissive metasurfaces, *Light: Sci. Appl.* **8**, 16 (2019).
- [25] X. Ling, X. Zhou, X. Yi, W. Shu, Y. Liu, S. Chen, H. Luo, S. Wen, and D. Fan, Giant photonic spin Hall effect in momentum space in a structured metamaterial with spatially varying birefringence, *Light: Sci. Appl.* **4**, e290 (2015).
- [26] Z.-Y. Tan, F. Fan, and S.-J. Chang, Active broadband manipulation of terahertz photonic spin based on gyrotropic Pancharatnam-Berry metasurface, *IEEE J. Sel. Top. Quantum Electron.* **26**, 1 (2020).
- [27] G. Milione, S. Evans, D. A. Nolan, and R. R. Alfano, Higher Order Pancharatnam-Berry Phase and the Angular Momentum of Light, *Phys. Rev. Lett.* **108**, 190401 (2012).
- [28] L. Zhang, S. Liu, L. Li, and T. J. Cui, Spin-controlled multiple pencil beams and vortex beams with different polarizations generated by Pancharatnam-Berry coding metasurfaces, *ACS Appl. Mater. Interfaces* **9**, 36447 (2017).
- [29] C. Zheng, G. Wang, J. Li, J. Li, S. Wang, H. Zhao, M. Li, Z. Yue, Y. Zhang, Y. Zhang, and J. Yao, All-dielectric metasurface for manipulating the superpositions of orbital angular momentum via spin-decoupling, *Adv. Opt. Mater.* **9**, 2002007 (2021).
- [30] J. Chen, F. Zhang, Q. Li, J. Wu, and L. Wu, A high-efficiency dual-wavelength achromatic metalens based on Pancharatnam-Berry phase manipulation, *Opt. Express* **26**, 34919 (2018).
- [31] L. Huang, S. Zhang, and T. Zentgraf, Metasurface holography: From fundamentals to applications, *Nanophotonics* **7**, 1169 (2018).
- [32] X. Zhang, S. Yang, W. Yue, Q. Xu, C. Tian, X. Zhang, E. Plum, S. Zhang, J. Han, and W. Zhang, Direct polarization measurement using a multiplexed Pancharatnam-Berry metahologram, *Optica* **6**, 1190 (2019).
- [33] L. Shao-he, L. Jiu-sheng, and S. Jian-zhong, Terahertz wave front manipulation based on Pancharatnam-Berry coding metasurface, *Opt. Mater. Express* **9**, 1118 (2019).
- [34] W. S. L. Lee, S. Nirantar, D. Headland, M. Bhaskaran, S. Sriram, C. Fumeaux, and W. Withayachumnankul, Broadband terahertz circular-polarization beam splitter, *Adv. Opt. Mater.* **6**, 1700852 (2018).

- [35] E. Hasman, V. Kleiner, G. Biener, and A. Niv, Polarization dependent focusing lens by use of quantized Pancharatnam–Berry phase diffractive optics, *Appl. Phys. Lett.* **82**, 328 (2003).
- [36] H. X. Xu, G. M. Wang, T. Cai, J. Xiao, and Y. Q. Zhuang, Tunable Pancharatnam–Berry metasurface for dynamical and high-efficiency anomalous reflection, *Opt. Express* **24**, 27836 (2016).
- [37] T.-T. Kim, H. Kim, M. Kenney, H. S. Park, H.-D. Kim, B. Min, and S. Zhang, Amplitude modulation of anomalously refracted terahertz waves with gated-graphene metasurfaces, *Adv. Opt. Mater.* **6**, 1700507 (2018).
- [38] J. Li, Y. Zhang, J. Li, X. Yan, L. Liang, Z. Zhang, J. Huang, J. Li, Y. Yang, and J. Yao, Amplitude modulation of anomalously reflected terahertz beams using all-optical active Pancharatnam–Berry coding metasurfaces, *Nanoscale* **11**, 5746 (2019).
- [39] See the Supplemental Material at <http://link.aps.org/supplemental/10.1103/PhysRevApplied.19.054086> for a detailed transmission-matrix derivation, simulation modeling, and experimental methods. It also includes Ref. [40].
- [40] H. G. Berry, G. Gabrielse, and A. E. Livingston, Measurement of the Stokes parameters of light, *Appl. Opt.* **16**, 3200 (1977).